

# The mass and dynamical state of Abell 2218

D. B. Cannon, T. J. Ponman & I. S. Hobbs

*School of Physics and Space Research, University of Birmingham, Birmingham B15 2TT, UK*

Accepted 1998 ??; Received 1998 ??; in original form 1997 ??

## ABSTRACT

Abell 2218 is one of a handful of clusters in which X-ray and lensing analyses of the cluster mass are in strong disagreement. It is also a system for which X-ray data and radio measurements of the Sunyaev-Zel'dovich decrement have been combined in an attempt to constrain the Hubble constant. However, in the absence of reliable information on the temperature structure of the intracluster gas, most analyses have been carried out under the assumption of isothermality. We combine X-ray data from the ROSAT PSPC and the ASCA GIS instruments, enabling us to fit non-isothermal models, and investigate the impact that this has on the X-ray derived mass and the predicted Sunyaev-Zel'dovich effect.

We find that a strongly non-isothermal model for the intracluster gas, which implies a central cusp in the cluster mass distribution, is consistent with the available X-ray data and compatible with the lensing results. At  $r < 1'$ , there is strong evidence to suggest that the cluster departs from a simple relaxed model. We analyse the dynamics of the galaxies and find that the central galaxy velocity dispersion is too high to allow a physical solution for the galaxy orbits. The quality of the radio and X-ray data do not at present allow very restrictive constraints to be placed on  $H_0$ . It is apparent that earlier analyses have under-estimated the uncertainties involved. However, values greater than  $50 \text{ km s}^{-1} \text{ Mpc}^{-1}$  are preferred when lensing constraints are taken into account.

**Key words:** galaxies: clusters: individual: A2218 – X-rays: galaxies – dark matter – cosmic microwave background – gravitational lensing – distance scale

## 1 INTRODUCTION

The masses of galaxy clusters can be determined in three main ways: using the velocity dispersion of the galaxies, the pressure gradient in the hot intracluster gas derived from X-ray imaging and spectroscopy, and by analysing the lensing of background galaxies by the cluster potential. Each of these approaches involve assumptions and are vulnerable to various systematic errors. It is therefore useful to compare the results of the different techniques. The X-ray and lensing approaches are generally considered the most reliable. Results from them have now been compared for a number of clusters (?). The agreement is often reasonable, but there are a few spectacular exceptions, of which Abell 2218 (hereafter A2218) is the most well studied example.

A2218 is an optically compact (core radius  $\approx 1'$ ; ?) cluster of galaxies, located at a redshift of 0.171 (?), and classified as richness class 4 (?). The cluster appears well relaxed, with the majority of the galaxies centred around the sole cD galaxy. However, detailed photometric studies (?; ?) suggest the existence of a second, smaller galaxy concentration, displaced from the cD by  $67''$ . Spectroscopic study (?),

performed on the central region ( $< 4'$ ) of A2218, has provided redshift information for 66 of the objects within the core and shown that the average velocity dispersion is  $1370 \text{ km s}^{-1}$ .

A succession of X-ray telescopes have allowed the properties of the hot gas within A2218 to be established. With the Einstein IPC & HRI (?) and ROSAT PSPC (?), the emission was found to be smooth (on scales  $\sim 1'$ ), azimuthally symmetric and centred on the cD galaxy. Fitting a polar profile of the surface brightness with a King model gave a core radius of  $58''_{-16}^{+16}$  and a  $\beta$ -value of 0.63 (?). Integrated spectral analyses with Ginga gave a gas temperature of  $6.72_{-0.4}^{+0.5} \text{ keV}$  and metallicity of  $0.2_{-0.2}^{+0.2} \text{ Z}_\odot$  (?). By virtue of Ginga's bandwidth, this determination is commonly accepted as the most accurate estimate of the mean gas temperature. Most recently, deep observations with the ROSAT HRI (?) have shown the presence of significant X-ray substructure within the cluster core, suggesting that the cluster may have undergone a recent merger event. This may account for the absence of any signs of a cooling flow in the cluster (?; ?).

Several previous comparisons (?; ?; ?; ?) between strong

lensing and X-ray analyses have found a factor of 2 discrepancy in the gravitating masses predicted by the two methods. Suggested explanations have centred upon the assumption of hydrostatic equilibrium for the cluster gas, the possibility that magnetic fields may provide significant pressure support to the gas and the presence of substructure within the cluster.

The Sunyaev-Zel'dovich decrement associated with A2218 has been extensively studied (??; ??; ??). These results have been used, in conjunction with X-ray data, to constrain the Hubble constant (??; ??; ??). These analyses have been made in the absence of reliable information about temperature variations in the intracluster gas and have therefore been forced to make simplifying assumptions, such as that of isothermality (??; ??; ??). This assumption is without a strong theoretical foundation and conflicts with the results of most cosmological simulations (??; ??; ??), which show temperature declining with radius, and mass distributions which have a central cusp. The question then arises as to whether simplifying assumptions have significantly biased the conclusions of previous X-ray analyses. For example, is the apparent discrepancy between the X-ray and lensing masses unavoidable or does it arise simply from the use of inappropriate assumptions in the X-ray analysis?

Motivated by the desire to avoid such restrictive assumptions, we have carried out an X-ray analysis which combines the capabilities of ROSAT and ASCA. The limited spectral bandwidth and resolution of the ROSAT PSPC is compensated for by the superior spectral properties of ASCA. Conversely, the poor spatial performance of ASCA is complemented by the higher spatial resolution of ROSAT. This approach has never before been applied to A2218.

The central aim of this paper is to improve our understanding of A2218 by comparing the results of our X-ray analysis with lensing, SZ and galaxy velocity studies. It also serves as a case study on the possible dangers of assuming an isothermal gas, when one has no information to the contrary. Throughout the paper we assume an Einstein-de Sitter cosmology with  $\Omega=1$ ,  $q_0=0.5$  and  $H_0 = 50 \text{ km s}^{-1} \text{ Mpc}^{-1}$ , except where otherwise stated.

## 2 X-RAY ANALYSIS

The objective of the analysis is to use spatially and spectrally resolved X-ray data to constrain models of the distribution of gas properties in the cluster. For an in-depth discussion of the procedures covered in this section, see ??.

### 2.1 Spectral-image modelling

We work with X-ray spectral images, which constitute blurred records of the spectral properties of the cluster projected along the line of sight. Since information about the disposition of material perpendicular to the plane of the sky is not available, it is necessary to make some assumption about the geometry of the source. We assume that the cluster is spherically symmetric. In practice, A2218 is slightly elliptical, with an axis ratio of 0.8 (??). However this modest ellipticity should not introduce any serious errors into our derived masses (??).

It is important to allow for the spatial and spectral blurring introduced by the telescope, as described by the instrument point spread function (psf) and energy response matrix. We adopt a forward fitting approach (??; ??), in which the properties of the gas are parameterised as analytical functions of cluster radius. The emission from each spherical shell in the cluster is computed using a ?, hereafter RS, hot plasma code. After correcting for cluster redshift, the spectral emissivity profiles are folded through the instrument spectral response, projected along the line-of-sight, rebinned into an  $xy$  grid and blurred with the psf. This produces a predicted spectral image which can be directly compared to the observed data, using a maximum-likelihood statistic. Iteratively adjusting the model parameters results in a best-fit to the data.

Using analytical forms for the radial distribution of gas properties has the advantage of regularising the solution (i.e. suppressing instabilities in the deprojection and deblurring processes), however one runs the risk that the solution may be dictated by the mathematical function imposed. This can lead to overconfidence in derived results, as acceptable alternatives which might fit the data are ruled out by the limitations of the available models. The commonly employed restriction of isothermality is an extreme example of this. We attempt to avoid this problem by using a range of radial functions. This is particularly important for the temperature and we use not only a number of parametric forms for  $T_{\text{gas}}(r)$ , but also an alternative approach in which  $T_{\text{gas}}(r)$  is determined indirectly, by fitting a model for the mass distribution, as discussed below. The gas density profile is much more readily determined by the X-ray data, so we have fitted only two radial forms.

Assuming that the intracluster gas is in hydrostatic equilibrium in the potential well of the cluster, the total gravitating mass within radius  $r$ , from the centre of the cluster, is related to the gas temperature and density by:

$$M_{\text{grav}}(r) = -\frac{kT_{\text{gas}}(r)}{G\mu m_p} \left[ \frac{d \ln \rho_{\text{gas}}(r)}{d \ln r} + \frac{d \ln T_{\text{gas}}(r)}{d \ln r} \right] r \quad (1)$$

where  $\rho_{\text{gas}}(r)$  is the gas density,  $T_{\text{gas}}(r)$  the gas temperature,  $\mu$  the mean molecular weight and  $m_p$  the proton mass.

#### 2.1.1 Gas density

The gas density is well constrained by the X-ray surface brightness, since the PSPC is largely insensitive to variations in temperature for  $T > 3 \text{ keV}$ . Surface brightness profiles are generally well fitted by core-index type models (??; ??):

$$\rho_{\text{gas}}(r) = \rho_{\text{gas},0} [1 + (r/r_c)^2]^{-\alpha_\rho} \quad (2)$$

where  $\rho_{\text{gas},0}$  is the central gas density normalisation ( $\text{amu cm}^{-3}$ ),  $r_c$  the core radius (arcmin) and  $\alpha_\rho$  the density index (unitless). The main deviations from this form occur at small radii, where cooling flows give rise to surface brightness cusps in many clusters, though not in A2218.

Recent N-body studies (??; ??; ??) have achieved good fits to dark matter (DM) and gas profiles in simulated clusters with an alternative description. The profiles are found to steepen progressively, from  $\rho_{\text{gas}}(r) \propto r^{-1}$  in the core, to  $r^{-3}$  near the virial radius, following the form

$$\rho_{\text{gas}}(r) = \rho_{\text{gas},0} [x(1+x)^2]^{-1} \quad (3)$$

where  $x = r/r_s$ ,  $r_s$  being the scale radius (arcmin). Both of the above analytical forms have been fitted to the X-ray data for A2218.

### 2.1.2 Gas temperature

The gas temperature distribution is less well determined, since this requires a combination of spatial and spectral resolution which has not generally been available in the past. We consider a variety of simple models: a linear temperature ramp (LTF),

$$T_{\text{gas}}(r) = T_{\text{gas},0} - \beta r \quad (4)$$

where  $T_{\text{gas},0}$  is the gas temperature (keV) at the cluster centre,  $\beta$  the temperature gradient (keV arcmin $^{-1}$ ) and  $r$  the radius (arcmin); a King-type temperature description (KTF),

$$T_{\text{gas}}(r) = T_{\text{gas},0} [1 + (r/r_T)^2]^{-\beta} \quad (5)$$

where  $r_T$  is the temperature core radius (arcmin) and  $\beta$  the temperature index (unitless); and a polytropic temperature description (TTF),

$$T_{\text{gas}}(r) = T_{\text{gas},0} [1 + (r/r_c)^2]^{\alpha_\rho(1-\gamma)} \quad (6)$$

where  $r_c$  is the gas density core radius (arcmin) and  $\gamma$ , the polytropic index (unitless), is fitted as a free parameter varying between isothermality ( $\gamma=1$ ) and adiabaticity ( $\gamma=5/3$ ).

### 2.1.3 Gravitating mass

An alternative to fitting  $\rho_{\text{gas}}(r)$  and  $T_{\text{gas}}(r)$  is to fit  $\rho_{\text{gas}}(r)$  and  $M_{\text{grav}}(r)$ . The corresponding temperature profile can then be inferred, via Equation 1. We use several alternative forms, motivated by the distribution of galaxies in clusters (?), and by the results of N-body simulations. These include: a core-index description (DMF),

$$\rho_{\text{DM}}(r) = \rho_{\text{DM},0} [1 + (r/r_c)^2]^{-\alpha_{\text{DM}}} \quad (7)$$

where  $\rho_{\text{DM},0}$  is the central dark matter density normalisation (amu cm $^{-3}$ ),  $r_c$  the core radius (arcmin) and  $\alpha_{\text{DM}}$  the density index (unitless); a model based upon the simulations of ? (DNF),

$$\rho_{\text{DM}}(r) = \rho_{\text{DM},0} [x(1+x)^2]^{-1} \quad (8)$$

where  $x = r/r_s$  and  $r_s$  is the scale radius (arcmin); and a Hernquist profile (DHF),

$$\rho_{\text{DM}}(r) = \rho_{\text{DM},0} / [2\pi b(1+b)^3] \quad (9)$$

where  $b = r/r_s$  and  $r_s$  is the scale radius (arcmin).

### 2.1.4 Fitting the models

Determination of the best-fit parameters for a cluster model proceeds in the way commonly employed for spectral fitting. The fit statistic employed is maximum likelihood, rather than chi-squared, since the data are generally strongly Poissonian. The fit and its local slope are determined at some initial position in the parameter space. This information is used to predict an improved set of model parameters and

the fit statistic re-determined. The process is iteratively repeated until the statistic slope falls below a pre-determined value. One limitation of this method is, however, that the fitting tends to follow the local gradient in the statistic, until it encounters a minimum. Thus the fit can become trapped in a “valley”, which it regards as the best-fit result, even though a more suitable combination of parameters may occur elsewhere. To avoid this, we randomly perturb models during analysis and force them to re-fit (to check if the same minimum is produced).

Confidence regions can be derived for each best-fit parameter, by offsetting the parameter of interest from its best-fit value (both above and below the best-fit), and re-optimising the other parameters. The resulting increase in the fit statistic, from its optimum value, is used to determine what offset would need to be applied in order to create a user-defined change in the statistic. This defines the required confidence interval. We use the form of the maximum likelihood statistic introduced by ?, such that changes in the statistic have the same significance as changes in chi-squared. Hence, for each parameter, an increase in the Cash statistic of 1 corresponds to a 68% confidence interval, and an increase of 2.71 to 90% confidence. The above process is repeated for each model parameter for which an error estimate is required.

Errors in physical quantities which are functions of radius (such as mass or temperature) are generally affected by several model parameters. We derive error envelopes for such quantities by taking the outer envelope of all of the curves generated by perturbing each free parameter to its upper and lower error bounds. Because these envelopes are derived using every parameter combination, each offset to their error bounds, the result is a *conservative* estimate of the statistical uncertainty.

Once the total gravitating mass distribution has been determined (using Equation 1, if the mass has not been modelled directly) the various mass components in the cluster can be separated. The gas mass profile is calculated from the fitted parameters. The galaxy mass profile can be constructed from the observed luminosity profile for the cluster, assuming a constant mass-to-light ratio. Subtraction of these components from the total mass profile then yields the dark matter profile.

## 2.2 ROSAT PSPC reduction

The aim of the ROSAT analysis is to obtain well constrained gas density parameters, which can then be utilised in the ASCA analysis.

The raw data, obtained on May 25th 1991, were reduced using the Starlink ASTERIX X-ray analysis package. Periods of high background were removed from the data, reducing the effective exposure time to 42 ksec but making the background subtraction substantially more reliable.

Subtraction of the X-ray background was accomplished by selecting data from an annulus ( $27' - 33'$ ), ignoring pixels covered by the detector support structure or containing point source emission. This background sample was then extrapolated to cover the whole field, using the PSPC energy-dependent vignetting function. Since the X-ray surface brightness profile for A2218 can be traced to a maximum radius of  $12'$ , the chosen background annulus is free of

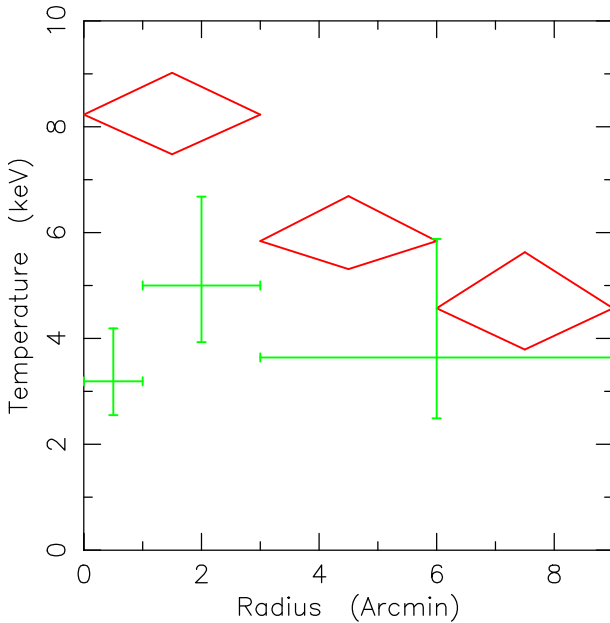


**Figure 1.** Gas temperatures derived in projected annuli. The barred crosses are taken from ROSAT PSPC analysis and the diamonds from ASCA GIS analysis. The results suggest a temperature decline with radius, with weak evidence (from the PSPC) for central cooling.

source emission. In the following analysis, the data are restricted to lie within  $9'$  to avoid possible systematic effects from uncertainties in the background subtraction at large radius.

The exposure-corrected, background-subtracted PSPC data were summed to provide an integrated cluster spectrum and split into concentric annuli, centred on the cluster core, within which spectra were extracted. Fitting these spectra gives an indication of the depth of the cluster potential well and the radial structure of the cluster gas density and temperature parameters (see Fig 1). However, any gradients present in these distributions will tend to be underestimated, due to the smoothing effects of the instrument psf and projection along the line-of-sight. Using annuli of width greater than the instrument psf minimizes the former effect.

In order to create a spectral image dataset, allowing a full spatial and spectral analysis, the data were formed into images of channel width 10, over the channel range 11–230 (approximately 0.2–2.3 keV). This results in a data cube, from which specific regions can be selected and analysed.

Within the cluster emission there is one bright source contaminating the data, located at a radius of  $11.1'$  from the cluster centre. In the PSPC analysis, the point source can be eliminated by ignoring the data collected in that region. However, this is not possible with ASCA, since the extended psf ensures that it is not discernable as a discrete source. To determine whether the source significantly affects our analysis, we model it using the PSPC data. The cluster emission is first fitted with the point source pixels removed. This model of the cluster emission is then subtracted from the original data, leaving behind just the point source, which is fitted with a power-law spectral model.

The fitted index, 1.25, indicates the softness of the

source - the majority of the flux is emitted below 0.5 keV. This is consistent with identification of the source as SAO17151, a bright star with a soft spectrum (?). If the PSPC-determined model for the point source is subtracted from the ASCA data, the cluster fits are modified to the extent that a 1.5% difference in the total gravitating mass at 2 Mpc results. This effect is negligible compared to other errors, so no attempt has been made to remove the source from the ASCA data.

### 2.3 ASCA GIS reduction

The ASCA analysis aims to constrain the gas temperature and metallicity profiles, using the PSPC derived gas density profile. A2218 was observed by the ASCA X-ray telescope on April 30th 1993. In this paper we use only data from the two gas imaging spectrometers (GIS2 and GIS3), since these have a wider field of view ( $\sim 50'$  diameter) and greater high-energy detector efficiency (up to 10 keV) than the CCD detectors (SIS0 and SIS1). An additional reason is that an accurate model for the large, asymmetrical and energy dependent psf is available for the GIS detectors, constructed from Cyg X-1 observations. These restrict analysis to a maximum radius of  $18'$  and an energy-range of 1.5–11 keV (?), which is not a significant limitation in the case of A2218.

Standard procedures for ASCA analysis, followed in this paper, are given by ?. The recommended screening criteria are applied to the raw data, removing data taken during times of high background flux. Subtraction of the X-ray background is complicated by the telescope psf. This has the effect of ensuring that no region of the detector is free from source flux. Hence, we extract an “average” background dataset from the publicly distributed set of blank-sky pointings (?). These datasets suffer from mild point-source contamination, as sources are not completely averaged out, but are currently the best available solution.

The results of a naive annular spectral analysis of the ASCA data are shown in Fig 1. However, it is important to bear in mind the limitations of this approach. Cross-talk between annuli is significant (?), and the energy-dependent spreading of flux results in a distorted temperature profile, such that analysis of a simulated isothermal cluster would give a temperature which rises with radius. In practice, the temperature appears to *decline* with radius, indicating that a real gradient is present.

For 3D analysis, spectral-image datasets with contiguous energy bands of width 50 raw channels are created. Since the cluster centre is offset from the detector centre, data beyond a radius of  $9'$  are not fitted (the offset added to the radial extent of the source is similar to the maximum radius where psf calibrations apply). This restriction minimises the effects of poor calibration and high background near the detector edge. As both GIS instruments behave similarly, the datasets are fitted simultaneously. The Cash statistic has been used to identify best-fit models, but similar results for best-fit parameters and for comparison between the quality of fit of different models, is obtained using the  $\chi^2$  statistic.

### 3 RESULTS

We first compare the results of our analysis with published studies, to investigate whether the fitted models are consistent with earlier work on A2218.

Integrated spectral analyses of clusters produce “mean” quantities which are representative of the entire object. Assuming isothermality, ? derived a gas temperature of  $6.72^{+0.5}_{-0.4}$  keV together with an iron abundance of  $0.2^{+0.2}_{-0.2}$   $Z_{\odot}$  (using an RS emission code, where all other heavy element abundances were fixed at  $0.5 Z_{\odot}$ ). This is in agreement with an earlier, much less well constrained examination (?). More recently, ? have derived  $T = 7.2$  keV and  $Z = 0.18 \pm 0.07 Z_{\odot}$ , from an integrated ASCA spectrum.

Fitting an RS model to our ROSAT data results in a gas temperature of  $4.7^{+1.1}_{-0.9}$  keV and a hydrogen absorption column of  $2.6^{+0.2}_{-0.1} \times 10^{20}$  cm $^{-2}$  (with metallicity fixed at the Ginga value). This absorption agrees with the Stark level of  $2.58^{+0.18}_{-0.18} \times 10^{20}$  cm $^{-2}$  (?). The temperature is lower than the Ginga result of ?, but the energy range of the PSPC is not very suitable for determining the temperature of such hot gas. It has been found previously (?) that PSPC results tend to be biased low for high temperature clusters. Fitting an integrated spectrum simultaneously to the GIS2 and GIS3 data gives a gas temperature of  $6.73^{+0.46}_{-0.44}$  keV and a metallicity of  $0.20^{+0.08}_{-0.08} Z_{\odot}$  (with the hydrogen column fixed at the PSPC value), in good agreement with the Ginga and ? results.

The ability to extract and analyse spectra from independent regions of the cluster represents a significant advance over analysis of the integrated emission. Fig 1 shows the derived annular temperature profiles from both ROSAT and simultaneous GIS2/GIS3 analysis. The PSPC results are consistent with ?, with a possible temperature drop visible in the central bin. However, the evidence for central cooling is statistically rather weak, and the derived central cooling time of  $\sim 1.5 \times 10^{10}$  yr is comparable with the Hubble time, so a strong steady-state cooling flow appears to be ruled out.

If the hydrogen column is fitted, using the PSPC data, it is found to be consistent with the Stark value (?) throughout the cluster, apart from a slight rise in the centre. This may be due to matter deposited by an earlier, disrupted cooling flow (as noted by ?). The ASCA analysis suggests that the metallicity may be slightly lower than the integrated value in the cluster centre with a shallow radial rise. However, all points are consistent with the ? value of  $0.2 Z_{\odot}$ .

Analysis using spectral-image datasets allows extraction of the 3D gas density and temperature distributions within A2218. In the subsequent cluster analysis, both ‘temperature models’ (fitting for  $\rho_{gas}(r)$  and  $T_{gas}(r)$ ) and ‘mass models’ (fitting for  $\rho_{gas}(r)$  and  $M_{tot}(r)$ ) are used. Parameters representing the metallicity and cluster position are also fitted.

The best constrained parameters derived from PSPC analysis pertain to the shape of the gas density distribution. Comparable analyses have been carried out using Einstein (?; ?; ?), and ROSAT (?) data. These studies agree that when a King profile is assumed, A2218 is well modeled with a core radius,  $r_c$ , of  $\sim 1'$  and an index,  $\alpha_{\rho}$ , of  $\sim 1$  (equivalent to a  $\beta$ -value of 0.67). Higher resolution analysis, using the ROSAT HRI, has been performed by ? and ?. These

studies detect the presence of smaller scale structure, with three surface brightness peaks visible within the central arcminute, none of which coincides with the central cD galaxy. This structure cannot be resolved with either the PSPC or GIS detectors, and indicates that the core of A2218 departs from a fully relaxed state.

Since ASCA is poor at constraining the gas density distribution for such a compact source, the PSPC fit values for core radius and index are carried over into the ASCA spectral-image analysis. To obtain the appropriate density parameters, a linear temperature ramp model is fitted to the entire PSPC data within a radius of 9 arcmin, with the temperature parameters fixed at those derived from an initial fit to the GIS data. This model is then re-fitted to the GIS data, complete to a radius of 9 arcmin, with the gas density core radius and index fixed, allowing a fit of the temperature parameters. In an iterative process, this model is alternately fitted to the PSPC and GIS datasets until no further change is observed in the parameter values. With consistency achieved, the “standard” gas distribution for A2218 is determined to be  $r_c = 0.91^{+0.03}_{-0.03}$  arcmin,  $\alpha_{\rho} = 0.96^{+0.02}_{-0.01}$ , in good agreement with the comparable results discussed above. If an NFW profile is assumed, the required scale radius,  $r_s$ , is  $10.27^{+0.21}_{-0.20}$  arcmin. However, the NFW parameterisation is neither preferred nor disallowed by the PSPC data, so we only use a King parameterisation for the gas density distribution in the following analysis.

#### 3.1 All cluster data

Fixing the gas density shape parameters at these King values, a range of models were fitted to the ASCA spectral-image data. On the basis of their Cash statistic, a set of models best-fitting the observed cluster data within a radius of 9 arcmin is selected (Table 1 lists the main parameters for each model) as representative of A2218. As can be seen from the Table, the isothermal model is a significantly poorer fit to the data. It is included for comparison with the other models. All of the temperature profiles obtained for this set (apart from that for the isothermal model) are plotted in Fig 2. Beyond the central arcminute ( $\sim 230$  kpc) the profiles are in good agreement and quite non-isothermal. The typical 90% confidence envelope for an individual model (remember that these are conservative envelopes) generally encompasses the spread of these best-fit profiles (a single error envelope is included to illustrate this point). Within the central region, which lies within a single ASCA psf, a greater spread in temperature is allowed by the data. However, despite this divergence in temperature at small radius, all of the best-fit models, bar the isothermal model, have similar Cash statistics (see Table 1).

The abundance of heavy elements has been assumed, in all of the above models, to be constant over the cluster. However, the spectral capabilities of ASCA allow us to test this assumption. Allowing a linear metallicity gradient with the best-fit linear temperature ramp model gives a slope of  $2.8^{+4.5}_{-6.5} \times 10^{-2} Z_{\odot}$  arcmin $^{-1}$ , a value consistent with uniform metallicity. The effect of this best-fit slope upon other model parameters is negligible, hence freezing the metallicity gradient at zero does not bias our analysis.

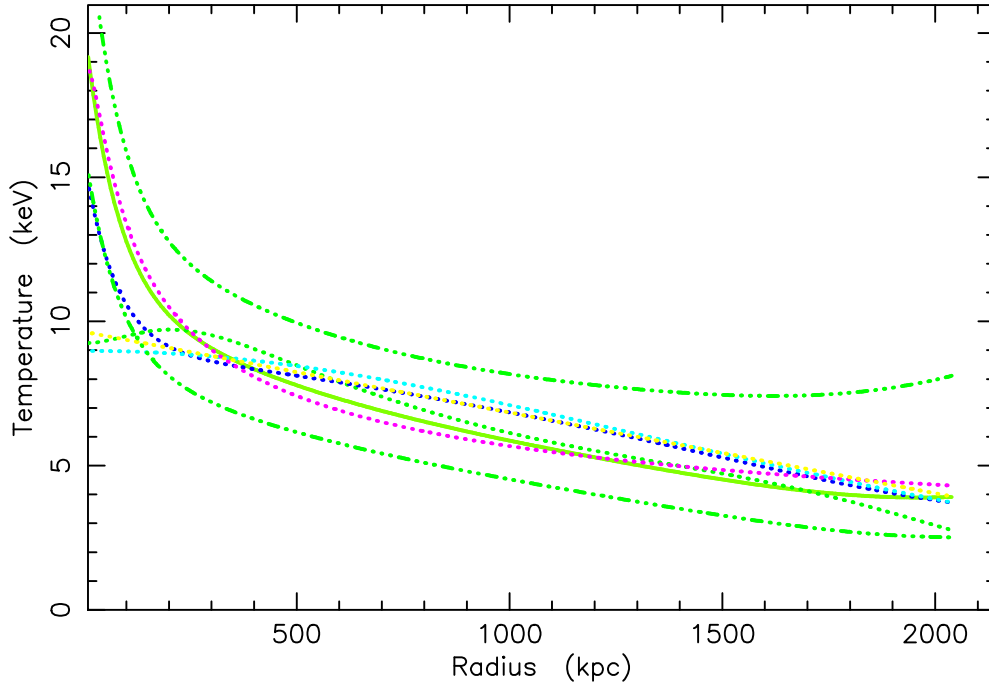


**Figure 2.** Fitted 3D temperature profiles for the cluster gas. The MMM (solid) is plotted together with its 90% error envelope (dash-dot) and the remaining best-fit models (dotted). All of the profiles feature gas temperatures which decrease by a factor of  $\sim 2$  or more within the region of analysis, and are consistent beyond the cluster core.

### 3.2 Central cluster data

We now examine the claim that lensing analyses require a larger cluster mass than is consistent with the X-ray data. The model which provides the greatest gravitating mass at the critical radius ( $\sim 85$  kpc) is therefore selected for examination. This model, the DHF best-fit, using a Hernquist description for the DM distribution and a King description for the gas density profile (see Table 1), implies a high central gas temperature. In the following comparisons, we refer to this model as the ‘‘maximum-mass model’’ (MMM).

The MMM temperature profile features a factor of 2 rise within the central  $1'$ . This raises two questions: does such a steep temperature gradient raise physical problems (would it be convectively unstable?), and is it consistent with the X-ray spectral data observed within the central region? We will return to the first question in Section 5.

To address the latter question, GIS3 spectra integrated within  $r = 1'$ , where the MMM temperature rises steeply, are compared with the predictions of the MMM and isothermal models in Fig 3. For clarity, only the energy range of 5–10 keV is displayed, since this is where the impact of very hot gas will be most apparent. Although the MMM provides a reasonable fit to the spectral imaging data *as a whole*, it does not follow that the data in the central regions need be consistent with the high model temperature. In practice, for both instruments (while the GIS2 spectra are not shown in Fig 3, they behave similarly to the GIS3 spectra) the MMM is a good match to the data. The isothermal model is, however, also consistent with the restricted dataset. The conclusion from this is that while the data do not rule out a central temperature rise, they do not require one either. The reason for this is that within the ASCA bandpass, plasmas

| Model Form | Central $T_{gas}$ (keV) | $T_{gas}$ Gradient (various) | Relative Cash Statistic |
|------------|-------------------------|------------------------------|-------------------------|
| LTF        | 9.64                    | 0.63                         | -636.08                 |
| LTF (ISO)  | 7.90                    | zero                         | -626.85                 |
| TTF        | 19.01                   | 1.20                         | -634.53                 |
| KTF        | 8.98                    | 3.18                         | -635.96                 |
| DNF        | 15.59                   | n/a                          | -636.12                 |
| DMF        | 9.24                    | n/a                          | -635.20                 |
| DHF (MMM)  | 20.42                   | n/a                          | -635.33                 |
| MMMC       | 16.44                   | n/a                          | -632.50                 |

**Table 1.** Temperature and statistic parameters for a variety of fitted 3D models are shown. Note that the MMMC is not a best-fit model in the same sense as the others, as is described in the text. For all models, the gas density core radius,  $r_c$ , and index,  $\alpha_\rho$ , are fixed at the values determined from the ROSAT data. Explanations for the model acronyms are given in the text.

with temperatures of 8 and 18 keV do not have substantially different spectral signatures and are thus difficult to differentiate (this is analogous to the difficulty that the PSPC has in dealing with clusters hotter than 2–3 keV). This problem is compounded by the limited spatial resolution of ASCA.

### 4 COMPARISON OF X-RAY AND LENSING MASSES

Deep optical observations of A2218 reveal a number of major arcs and a wealth of minor arclets. These features are the result of gravitational lensing, an effect which is independent

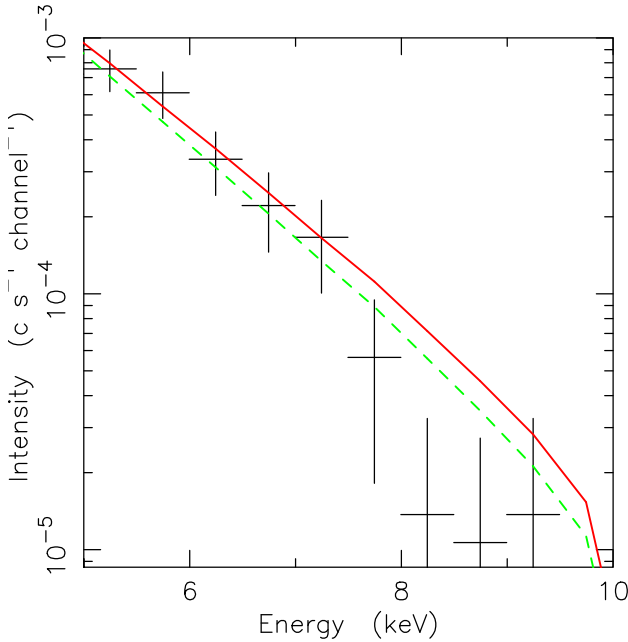


**Figure 3.** The GIS3 spectrum from the central 1' (crosses) is compared to the prediction from the MMM model (solid) and the isothermal model (dashed). The MMM model provides more flux at high energy, because of the centrally increasing temperature, but the difference is very small. Both models are consistent with the observed data.

of the physical state of the cluster gas. Instead, uncertainty lies in the characteristics of the background galaxies and the possibility of matter sub-clumps along the line-of-sight.

Using the models fitted to A2218, we can derive projected gravitating mass profiles, suitable for comparison with the results of lensing analysis. This involves assuming a maximum outer radius for the cluster mass distribution. In the following analysis we take this to be the maximum radius of the data used in cluster fitting, which is 9' ( $\sim 2$  Mpc). The choice of projection radius has a minor impact upon the derived projected mass profiles (compared to other uncertainties) so long as the chosen radius is sufficiently large,  $\geq 2$  Mpc. For example, the difference in projected mass within 2 Mpc, between models with maximum radii of 2.0 and 3.0 Mpc, is 9%.

Since lensing analysis measures the matter distribution on both small (strong lensing occurs where the surface mass density is high) and large (weak lensing is theoretically observable to the edge of the cluster) scales, comparison with X-ray results is extremely informative. In Fig 4 the X-ray derived projected mass profiles for the MMM and isothermal model are plotted, together with the lensing results of ?, ? and ?.

#### 4.1 Strong lensing

Strong lensing analysis has been performed, using spectroscopically observed arcs, by a variety of groups (?, ?, ?, ?, ?). These analyses provide the gravitating mass within the critical radius associated with the formation of giant arcs, which in A2218 is 22.1" ( $\sim 85$  kpc).

The two strong lensing points, plotted in Fig 4 at this

radius, are consistent with a projected mass of  $\sim 6 \times 10^{13} M_{\odot}$ , despite their use of different mass distributions (assume a bipolar mass model while ? use an isothermal sphere distribution). The corresponding projected mass for the MMM is  $5.3_{-4.1}^{+1.2} \times 10^{13} M_{\odot}$ . The uncertainty associated with this mass is large enough to include the lensing derived value, so, within the calculated errors, the X-ray and strong lensing analyses are consistent, when the MMM is used. The corresponding mass from the isothermal model is  $2.8_{-0.2}^{+0.2} \times 10^{13} M_{\odot}$  (see Fig 4), in agreement with the factor of 2 discrepancy reported by previous analyses (?, ?, ?).

The bipolar mass model of ? was used by these authors to extract a further two masses (see Fig 4), at the radius of the second mass clump (256 kpc) and at the maximum radius where giant arc constraints can be applied (383 kpc). The projected, enclosed gravitating mass at these radii for both the MMM and the isothermal model are given in Table 2. No error estimates are given by ? for the lensing masses. However, it can be seen that both of these outer lensing points lie just outside the statistical error envelope of the MMM, unlike the mass derived at the critical radius. This is due to the MMM profile flattening at large radius. Note however that both of the outer predicted masses depend upon the bimodal model of ?, whereas the inner point can be derived in a model-independent fashion.

The ? bimodal mass model has received additional support from detailed optical observations by ?. In this analysis, the redshift of one of the faint arcs was determined for the first time and found to be in good agreement with the value predicted by ?.

The conclusion which can be drawn from this X-ray/strong lensing comparison is that it is *not* clear that the results from the two approaches are inconsistent. We have shown that when a model such as the MMM is used, which includes a central mass cusp, the predicted masses at the critical radius agree within the X-ray statistical error envelope (see Table 2). If the gas is assumed to be isothermal, the previously noted discrepancies can be reproduced (see Fig 4).

#### 4.2 Weak lensing

A statistical analysis of the weakly lensed arclets has been carried out by ?, allowing the slope of the surface mass density to be mapped within a radius of  $\sim 1$  Mpc. Fig 4 shows that, within errors, the magnitudes of the weak lensing points are consistent with the MMM. However, the trend indicated by these points is for a steeper profile, providing more gravitating mass at large radii than predicted by the MMM.

A significant difficulty with the weak lensing analysis, noted by ?, is the procedure used for normalisation. This is done by defining a reference annulus at large radius within which the cluster mass contribution is assumed to be negligible. Since the annulus used by ? has an inner radius of 800 kpc, while the X-ray surface brightness profile can be traced to  $r > 2$  Mpc, some shear signal from the cluster must actually be present within the reference annulus. Hence the recovered normalisation is an underestimate, such that the weak lensing mass profile can only be regarded as a lower bound to the projected mass. The impact of this is examined further in Section 6. The correction for this effect has

| Source/Mass   | 85kpc (x10 <sup>13</sup> M <sub>⊙</sub> ) | 256kpc (x10 <sup>14</sup> M <sub>⊙</sub> ) | 383kpc (x10 <sup>14</sup> M <sub>⊙</sub> ) |
|---------------|---|--|--|
| Kneib 1995    | 6.1                                       | 2.7  | 4.5  |
| Loeb&Mao 1994 | 6.4                                       | -  | -  |
| MMM           | 5.3 <sup>+1.2</sup> <sub>-4.1</sub>       | 2.0 <sup>+0.5</sup> <sub>-1.6</sub>        | 3.0 <sup>+0.7</sup> <sub>-2.4</sub>        |
| Isothermal    | 2.8 <sup>+0.2</sup> <sub>-0.2</sub>       | 1.6 <sup>+0.2</sup> <sub>-0.1</sub>        | 2.8 <sup>+0.1</sup> <sub>-0.1</sub>        |

**Table 2.** Projected gravitating masses from strong lensing and X-ray analysis are compared at the radii used by ?. At the critical radius the isothermal mass is a factor of 2 too low, although the discrepancy reduces greatly at larger radii.

been estimated by ? to be a factor of  $\sim 1.2$ - $1.6$  in projected mass.

If the weak lensing points are adjusted to take account of this factor, this has two important implications for the MMM comparison. First, the normalisation of all data points increases, bringing the inner points into better agreement with the MMM profile while the outer points move further from consistency. Second, because this adjustment is a DC effect for the reconstructed projected surface mass density (of the cluster), it does not act equally on the radially integrated points. Hence, when the normalisation is raised, the slope of the weak lensing mass profile in Fig 4 *increases*, bringing it into greater conflict with the MMM profile. Thus the flatter slope of the MMM cannot be made consistent with the weak lensing points by shifting the reference annulus to larger radii.

Even when the normalisation adjustment is applied, this is insufficient to ensure full consistency with the outer strong lensing points of ?, which (see Table 2) lie above the values of  $1.5 \times 10^{14}$  M<sub>⊙</sub> and  $2.5 \times 10^{14}$  M<sub>⊙</sub> predicted at the same radii by weak lensing. There is, however, a well understood effect whereby the weak lensing signal is suppressed at small radii due to contamination by cluster galaxies, reducing the derived weak lensing mass (?; ?). Correcting for this would bring the inner weak lensing points into greater consistency with both the strong lensing and X-ray results.

Overall, then, this comparison indicates that at large radii,  $> 250$  kpc, the weak lensing and X-ray analyses are reasonably consistent, though the weak lensing results tend to give more mass at large radii. Further work (observations of increased numbers of arclets over a wider field) is required to reduce the uncertainty in the weak lensing analysis and to move the reference annulus to larger radii, where the cluster mass contribution is lower.

## 5 GAS ENTROPY

In Fig 5 the derived gas entropy profiles for the best-fit cluster models are plotted. These indicate that beyond a radius of  $\sim 120$ kpc the entropy increases with radius, as is expected for gas which is convectively stable. However, within this radius three of the best-fit models (including the MMM) exhibit a slight inward rise in entropy, making the gas convectively unstable. For the MMM, the predicted increase in entropy which occurs between a radius of 120kpc and the cluster centre is  $\sim 30\%$ . The reason for this behaviour is that the temperature increases rapidly at small radii while the gas density is forced to flatten (due to the use of a King model description). However, it is precisely this temperature

increase that allows the model to achieve consistency with the gravitational mass derived from strong lensing.

As noted in Section 3, the NFW gas parameterisation is neither preferred nor disallowed by the PSPC data. However, if the King gas density parameterisation used for the MMM is replaced by the NFW parameterisation, the central entropy drops by  $\sim 75\%$  (See Fig 5). This difference is large enough to ensure that entropy rises continuously at all radii, removing the problem of convective instability.

## 6 CENTRAL GALAXY MASS

An alternative method for bringing the strong lensing and X-ray analyses into agreement has been examined by ?. In this study, a massive central galaxy was embedded within the cluster to increase the predicted core mass without violating observational X-ray constraints. As the cD galaxy envelope can be traced to at least  $25''$  (96kpc), which encompasses the critical radius, this is potentially an important consideration.

? tested this hypothesis by, firstly, constructing a total mass distribution which included both cluster and cD components. These were parameterised by a King mass model (equation 7 with  $\alpha_{\text{DM}} = 3/2$ ) and an isothermal sphere mass model ( $\alpha_{\text{DM}} = 1$ ), respectively. Secondly, the gas temperature distribution was constrained to be isothermal at large radius (beyond the cD galaxy) and to rise or fall linearly with  $r$  at small radius. By assuming the gas to be in hydrostatic equilibrium, the gas density distribution corresponding to different temperature models was extracted and compared to the observed Einstein surface-brightness data.

Constraining the temperature to be isothermal at  $r > 31''$ , at the ? derived value, ? found that models consistent with both the X-ray surface brightness and with enough central mass to account for the strongly lensed arcs had two notable features. Firstly, a cD component was required to ensure that the critical surface mass density was attained by the model. Secondly, the gas temperature rose sharply within  $31''$ , reaching a central value of  $\sim 11$ keV. Models which did not include a cD mass contribution, or which assumed the gas to be isothermal at all radii, were unable to provide sufficient mass at small radii to account for the lensing data, whilst remaining consistent with the Einstein data.

The projected gravitating mass within 1.5 Mpc, from the model favoured by ?, of  $1.3 \times 10^{15}$  M<sub>⊙</sub> is in reasonable agreement with the MMM value of  $9.0^{+1.4}_{-5.3} \times 10^{14}$  M<sub>⊙</sub>. This consistency is also found at smaller radii,  $r=100$  kpc, where ? obtains a mass of  $5.2 \times 10^{13}$  M<sub>⊙</sub> compared to  $6.6^{+1.5}_{-5.1} \times 10^{13}$  M<sub>⊙</sub> for the MMM. It should be noted that the MMM employs

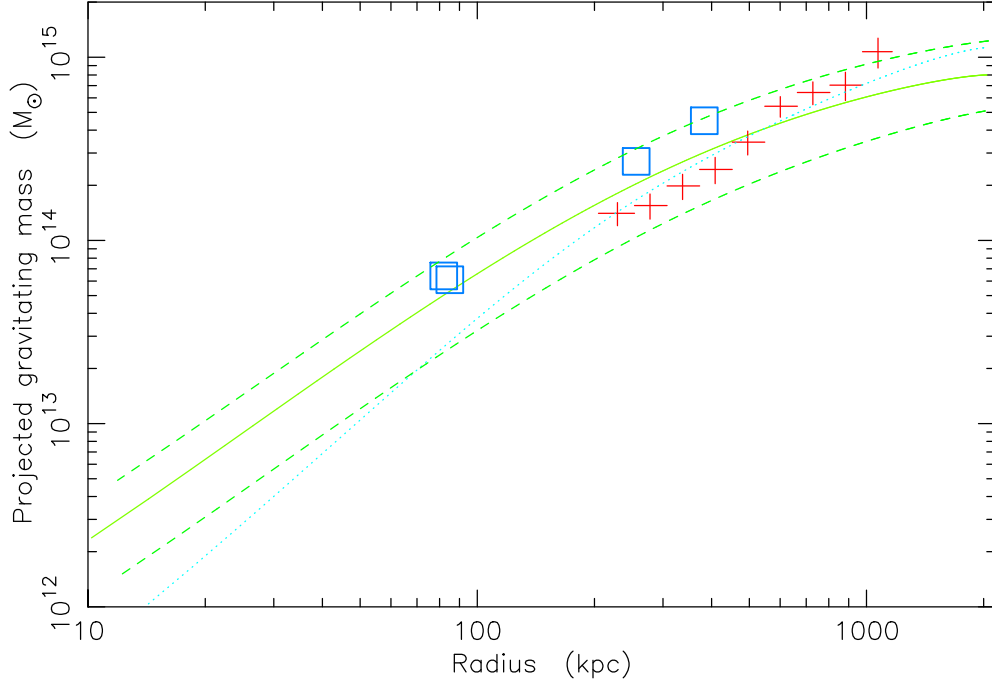


**Figure 4.** Projected gravitating mass profiles for the MMM (solid line) and isothermal (dotted line) are plotted. Also shown is the 90% error envelope for the MMM (dashed lines). Overlaid are strong lensing points from ? and ? (boxes) together with the weak lensing points of ? (crosses).

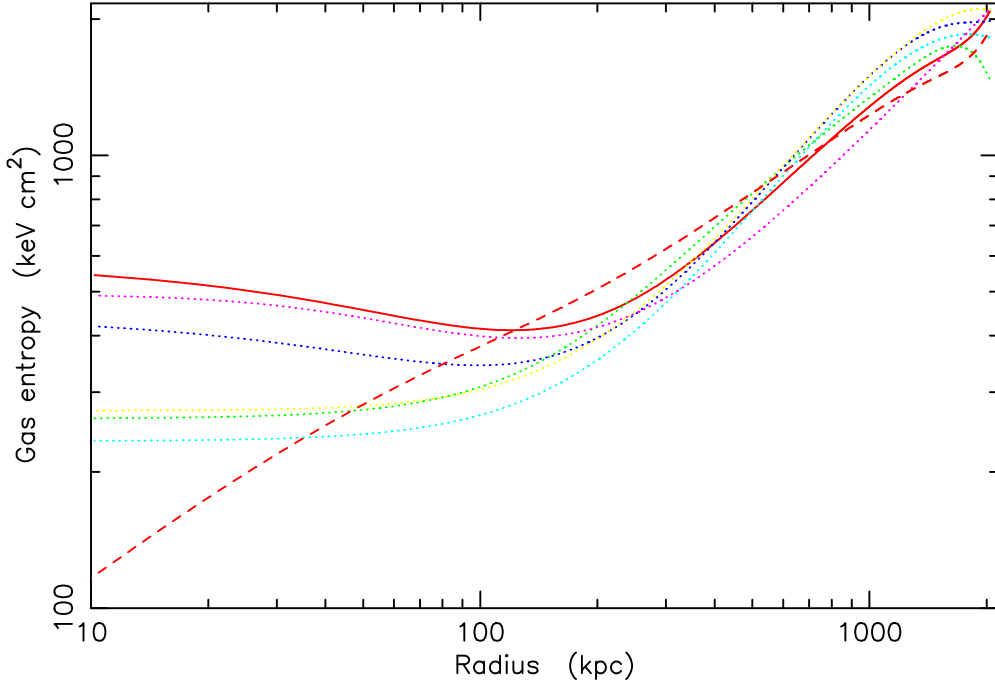


**Figure 5.** Derived entropy profiles for the cluster gas. The MMM is plotted for both a King (solid) and an NFW (dashed) gas density distribution. The remaining best-fit models (dotted) are plotted using the King parameterisation. It can be seen that all of the models are consistent with a gas which is convectively stable, except within  $\sim 120$  kpc, where the high central gas temperatures of certain models (such as the MMM, see Table 1) lead to an increase in entropy. Where the NFW gas density form is used, the derived entropy increases at all radii.

a mass profile with a central mass cusp ( $\rho_{\text{DM}} \propto r^{-1}$ ) but does not include any discrete component corresponding to the central galaxy. We now explore the effect of adding such an additional central component to our model.

Adding a central galaxy of radius 100kpc and adjustable mass normalisation to the MMM, we find that the statistical quality of the fit deteriorates. The largest additional mass allowed, at the 95% level, is  $1.7 \times 10^{12} M_{\odot}$  (within 100kpc). From here on this model is referred to as the MMMC, since it represents the MMM plus a central galaxy mass. Note however that the MMM, which contains no central mass component, is still statistically preferred (see Table 1).

This central mass is substantially less than the ? value of  $5.2 \times 10^{13} M_{\odot}$  (recall, however, that our cluster profile contains a central cusp, whilst Makino's has a flat core). Compared to the MMM, it provides a mass increase at the critical radius of only  $\sim 5\%$ . However, whilst the addition of a central mass component has little impact at small radius, it has the rather counter-intuitive effect of providing more mass at *large* radius. The reason for this is that, in the case of the MMM, the DM distribution has a scale radius of  $1.89^{+0.06}_{-1.16}$  arcmin. When a central mass component is added, the DM profile no longer needs to peak so sharply and its scale radius increases to  $6.79^{+0.95}_{-1.49}$  arcmin.

Fig 6 shows the MMM and MMMC mass profiles compared to the strong and weak lensing results. It can be seen that the increased mass of the MMMC at large radius (compared to the MMM) allows it to be consistent, within its 90% statistical confidence envelope, with both the two outer points derived by ? and the weak lensing points of ?.

We can use our models to estimate the baseline error involved in the weak lensing analysis, as a result of cluster mass residing within the reference annulus employed by ?. In Fig 6 the result of using the MMMC to correct the weak lensing results for this mass is also plotted. It can be seen that the points come into better agreement with the MMMC profile, particularly at  $r \gtrsim 500$  kpc. At smaller radii the weak lensing points still lie systematically below the MMMC profile, although this is to be expected (see Section 4.2) due to dilution of the lensing signal by cluster galaxies.

In Fig 7 the derived gas entropy profile for the MMMC is compared with those from the best-fit X-ray models within the central 500kpc region, where the MMM shows a noticeable rise. It can be seen that the MMMC provides a flatter central entropy distribution, such that the gas is less likely to be subject to convective instability.

## 7 ANALYSIS OF GALAXY MOTIONS

The dynamics of cluster galaxies provide a further way of investigating the mass distribution in clusters. In the case of A2218, galaxy redshifts are available only within a few core radii of the centre. However this includes the region where the lensing analysis of ?, and the high resolution X-ray observations of ?, suggest that the potential may be seriously disturbed.

Galaxy velocity and position data have been obtained from the NASA Extragalactic Database. This consists largely of the data obtained by ?, who performed an extensive photometric survey of the cluster core. On the basis of the  $3\sigma$  clipping technique of ?, 49 of the 53 galaxies with

measured redshifts are identified as cluster members. All of these galaxies lie within  $3'$  of the X-ray centroid of the cluster, which has been adopted as the centre for this optical analysis. The average line of sight velocity dispersion, calculated using the 49 cluster galaxies, and corrected (?) to the cluster rest frame, is  $1354^{+176}_{-118} \text{ km s}^{-1}$ .

This galaxy distribution has been studied using the techniques described by ?, using the Jeans equation to relate the spatial and velocity distribution of the galaxies to the gravitating mass profile for the cluster. The aim of such an analysis is to determine the radial behaviour of the anisotropy in the galaxy velocity distribution, since no information about galaxy orbits is otherwise available. Since the radial distributions of galaxy density and velocity are projected along the line of sight, the analysis requires an extrapolation to large radius of the X-ray determined mass profile, the galaxy velocity dispersion profile and the galaxy surface density profile. Extrapolating the galaxy profiles is particularly uncertain because data only extend out to  $\sim 2'$  ( $\sim 500$  kpc) and include no information (except in projection) regarding the behaviour of these profiles beyond this region.

The anisotropy is studied through  $\beta$ , the anisotropy parameter, which is 1 in the case of purely radial orbits, 0 for an isotropic velocity distribution and increasingly negative as the orbits become predominantly circular, with the limiting case of  $-\infty$  for purely circular orbits. It is unlikely, however, that the full range of allowed values of  $\beta$  is covered in any cluster. On the basis of numerical simulations, ? found that over the lifetime of most clusters, anisotropies corresponding to a  $\beta$  more negative than -1.5 are unlikely to have had time to develop.

For the galaxy surface density profile, a standard modified-Hubble profile ( $\Sigma = \Sigma_0 [1 + (r_p/r_c)^2]^{-1}$ ), with a canonical core radius of 250 kpc, has been used. The same parameterisation has been adopted by ?, who carried out an analysis rather similar to that presented here. The line of sight velocity distribution has been fitted by a linear ramp model using a maximum likelihood method. The best-fit has a central velocity dispersion of  $1478^{+345}_{-321} \text{ km s}^{-1}$ , while the gradient, although consistent with zero, is such that the dispersion falls with radius at a rate of  $-114^{+257}_{-240} \text{ km s}^{-1} \text{ arcmin}^{-1}$ .

The results of the analysis are shown in Fig 8, in which the calculated anisotropy parameter profiles for both of the most interesting X-ray mass models (the MMM and MMMC) are shown. Although the shape of the MMMC anisotropy profile is in detail different from those presented by ?, the conclusion is the same - there is a divergence in the degree of anisotropy in the core of A2218. This is a result of the high central line of sight velocity dispersion being inconsistent with the mass provided by either the MMM or MMMC.

In our anisotropy profiles, the anisotropy plummets to  $-\infty$  at a non-zero radius (within the central  $\sim 1'$  in the case of the MMMC model) and within this radius the solution is unphysical, requiring an imaginary velocity dispersion. There are two possible reasons for this. Firstly, in comparison with other clusters, A2218 has an unusually large central velocity dispersion. Numerical simulations (?) have shown that the velocity dispersion can increase by up to a factor of 2 during a merger event. This occurs during the violent

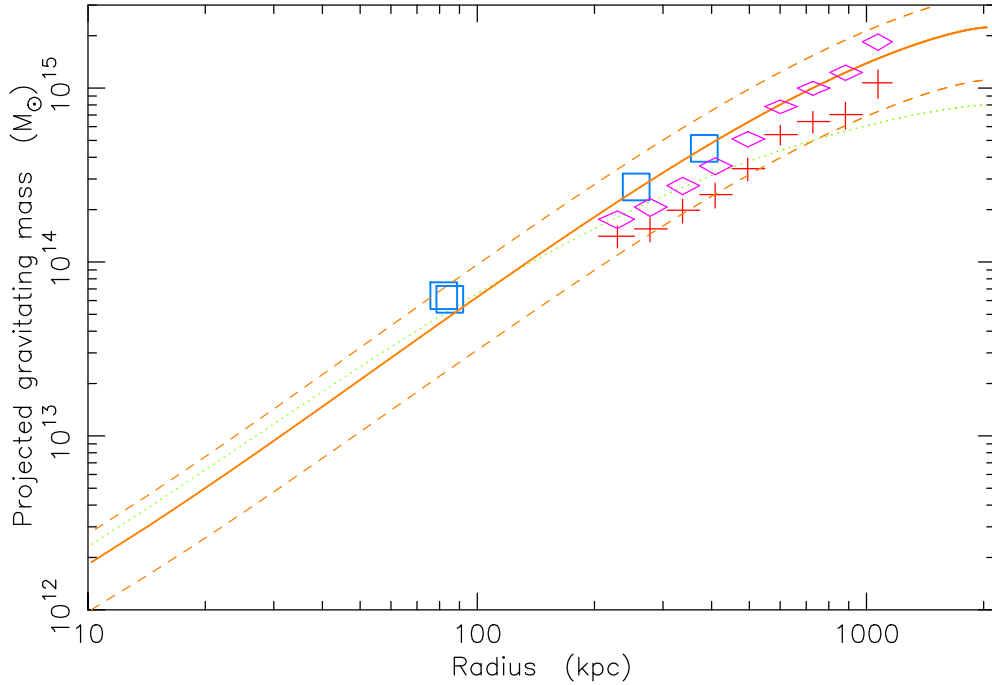


**Figure 6.** The projected gravitating mass profile for the MMM (dotted line) is compared with that of the MMMC (solid line). Also shown is the 90% error envelope for the MMMC (dashed lines). Overlaid are the strong lensing points from ? and ? (boxes) together with the weak lensing points of ? (crosses). Also shown are the weak lensing points after correction for cluster mass (as predicted by the MMMC) within the lensing reference annulus (diamonds). It can be seen that the MMMC provides a good match to both the strong and weak lensing points (especially after re-normalisation of the latter).

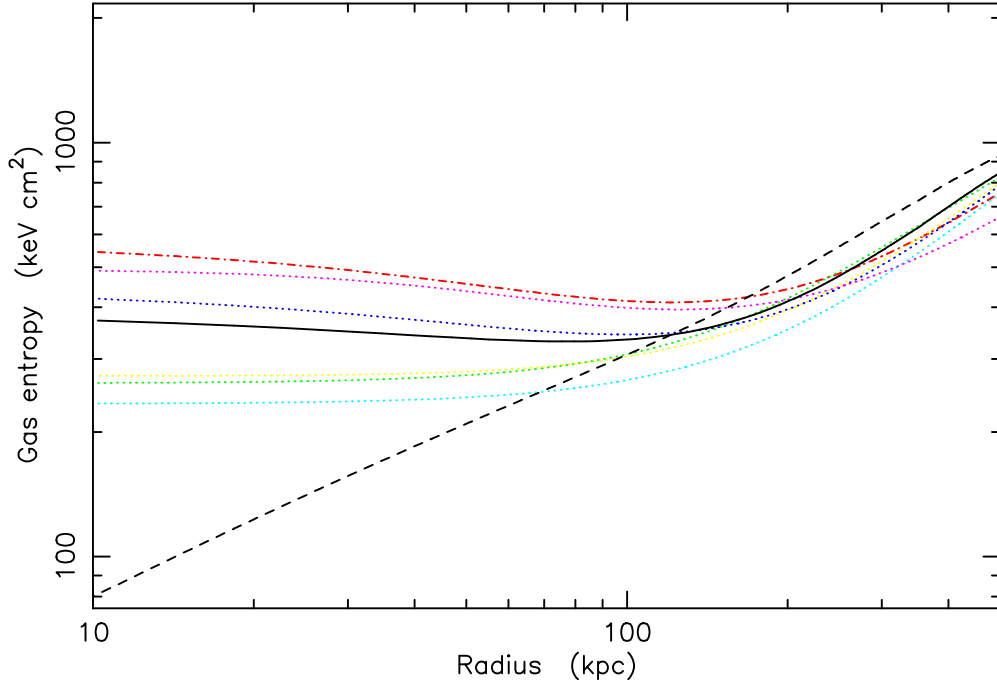


**Figure 7.** Derived gas entropy profiles for the inner 500 kpc region are plotted. The MMMC (solid line) can be seen to provide a considerably flatter central entropy profile than the MMM model (dash-dot line), where both use a King model for the gas density. If an NFW gas density form is used with the MMMC (dashed line), the derived entropy can be seen to increase at all radii. The remaining best-fit model profiles (dotted) are included for comparison.

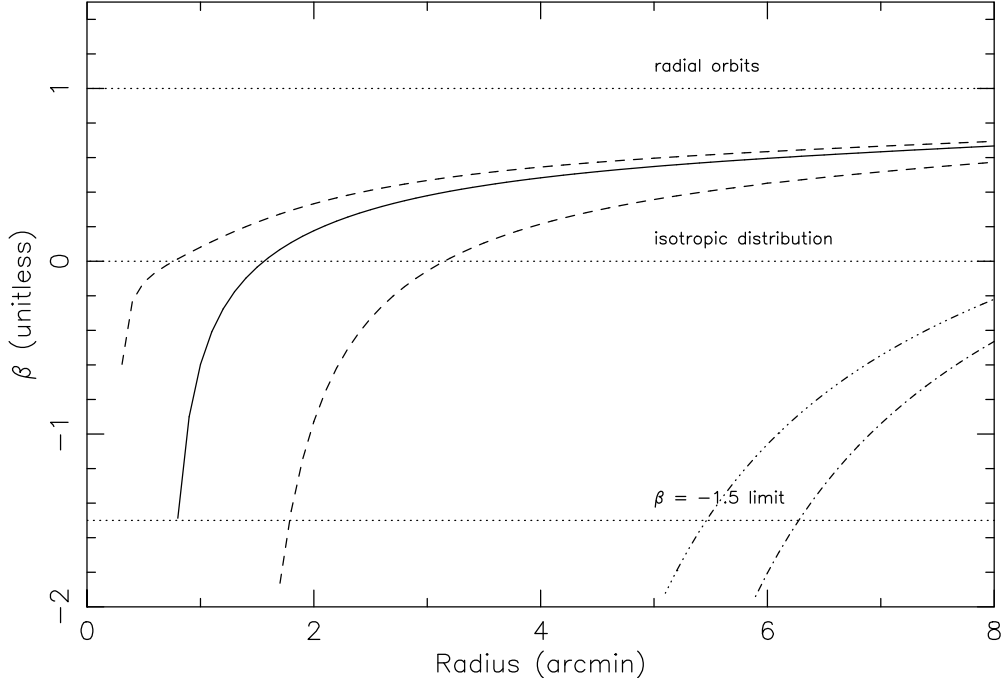


**Figure 8.** The anisotropy parameter for the two mass models discussed in the text is plotted as a function of radius. The anisotropy derived using the MMMC mass profile is indicated by the solid line, together with its 90% uncertainty envelope (dashed lines). The MMM (dash-dot line) is shown together with its upper error bound (dash-3dot line) only, since the lower bound is unphysical at all radii. The MMMC is acceptable at  $r \gtrsim 1'$ , while the MMM is only allowed at radii beyond the observed edge of the optical data. Both models predict predominantly radial orbits at large radius. The  $\beta = -1.5$  limit refers to the constraint from simulations (referred to in the text) that anisotropies more negative than  $-1.5$  should not have had time to develop.

relaxation phase of the merger. At this time, the assumptions underlying any analysis based upon the Jeans equation are invalid. This provides one way in which the unphysical behaviour of the anisotropy parameter can be understood.

Secondly, the unphysical values of  $\beta$  may be indicating that the spherically symmetric model and assumptions that our solution uses may be in error. This is supported by several sets of independent evidence which suggest that the cluster core is disturbed, on the scale of  $\sim 1'$ . ? find that the strong lensing data require a bimodal potential, ? uses high-resolution X-ray data to indicate that the cluster strongly deviates from spherical symmetry in the core and recently ? showed that the combined galaxy spatial and redshift data indicate the presence of two merging galaxy sub-clumps. Thus, there are good reasons to believe that A2218 has recently undergone a merger event, upsetting the virial equilibrium in the cluster core.

In the case of the MMM model, the solutions are unsatisfactory throughout the region for which galaxy data are available, such that a more widespread upheaval would be required to account for the high velocity dispersion.

## 8 SUNYAEV-ZEL'DOVICH EFFECT

The Sunyaev-Zel'dovich microwave decrement (?) results from inverse-Compton scattering of cosmic background photons by electrons in the cluster gas. The magnitude of the effect depends upon the integral of the gas pressure along the line of sight and hence has a different dependence on gas

density than the X-ray surface brightness. By combining an analysis of the X-ray emission with the observed SZ effect, it is possible to determine the distance of the cluster, and hence  $H_0$ . Recent measurements (?; ?; ?) have been used to place constraints upon the Hubble constant in this manner. ? measure the decrement in a linear strip across the cluster, deriving the 1D profile. ? and ? work with 2D images of the decrement, allowing construction of a parameterised model for the observed microwave decrement.

Several different observations of the decrement for A2218 have been combined with X-ray data, assuming an isothermal plasma, to constrain  $H_0$  (?; ?; ?; ?). The results obtained vary widely, with the most disparate estimates being  $24_{-10}^{+23} \text{ km s}^{-1} \text{ Mpc}^{-1}$  (?) and  $65_{-25}^{+25} \text{ km s}^{-1} \text{ Mpc}^{-1}$  (?).

In Fig 9 the predictions of our X-ray analysis are compared with the measurements of ? and the allowed envelope of ?, assuming  $H_0 = 50 \text{ km s}^{-1} \text{ Mpc}^{-1}$ . The typical statistical uncertainty for a single model is similar to the scatter between the best-fit model predictions; both of these are small compared to the SZ error envelope.

At radii greater than 100 kpc, the observed and predicted decrements are in excellent agreement. However, at smaller radii, the decrement observed by ? lies significantly below the X-ray model predicted profiles. Limitations inherent to beam-switching single-dish measurements are that they are prone to baseline errors and beam dilution. Thus our analysis is not based upon the ? data, but instead makes use of their results only to allow a comparison with earlier studies.

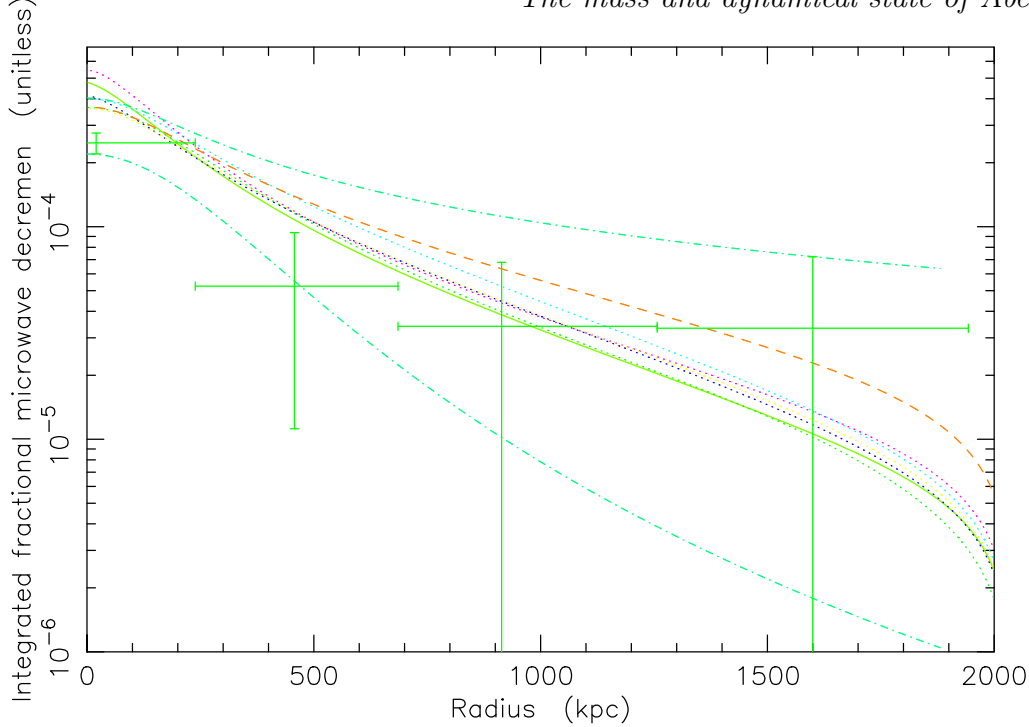


**Figure 9.** Sunyaev-Zel'dovich decrement profiles predicted from the MMM (solid line) and best-fit cluster models (dotted lines), together with the decrement which occurs when an isothermal model is used (dashed line). The observed results of ? (crosses) and ? (dash-dot line) are overlaid. A Hubble constant of  $50 \text{ km s}^{-1} \text{ Mpc}^{-1}$  is assumed.

These problems are not shared by the observation of ?, whose calculated envelope encompasses both the ? observations and the majority of the predicted profiles for  $H_0=50 \text{ km s}^{-1} \text{ Mpc}^{-1}$ , with the MMM being an important exception. This discrepancy occurs because the MMM requires a steep gas temperature gradient at small radii (see Fig 2), resulting in a high prediction for the central decrement. If the gas is assumed to be isothermal (which is not statistically allowed by our X-ray data) the predicted SZ decrement at large radius is significantly greater than that from the best-fit ASCA models (see Fig 9). However, the isothermal model cannot be discriminated against on this basis as it remains consistent with the large SZ error envelope.

If an alternative value of  $H_0$  is assumed, the predicted decrements obtained from the best-fit X-ray models can be varied to achieve consistency with the SZ observations. The dependency is such that for a given X-ray surface brightness, the predicted SZ decrement varies as  $H_0^{-0.5}$ . Hence, assuming a higher Hubble constant will lead to a lower X-ray predicted decrement. The 2D SZ observation of ? and ? is ideal for such a comparison because, first, it avoids the uncertainty inherent in the ? analysis and, second, upper and lower bounds to the allowed decrement are derived. However, it should be noted that these decrements have been analytically parameterised to allow a fit to the mosaiced SZ image and hence include a degree of model dependence (?). With this caveat in mind, it is possible to determine the range of  $H_0$  allowed by the SZ and X-ray results.

Under the requirement that at least one of the ASCA best-fit models must be consistent with the results of ?, we find that  $H_0$  can be limited to the very conservative range  $37-230 \text{ km s}^{-1} \text{ Mpc}^{-1}$ . The lower bound is obtained by de-

termining what value of  $H_0$  is required to make the SZ prediction from the LTF model (which predicts the lowest central decrement of any of the models) equal to the ? upper bound. The upper bound, which is clearly ruled out by other  $H_0$  determinations, is obtained by determining the value of  $H_0$  which would decrease the SZ prediction from the TTF model (which provides the highest central decrement of any of the models) such that it matches the ? lower bound. Using a value of  $H_0$  outside these bounds results in all of the ASCA best-fit models becoming inconsistent with the SZ observations.

The main conclusion of this analysis is that only weak constraints on the Hubble constant can be obtained, with even the very low ? result being allowed within its errors.

However, this determination neglects an important additional constraint, namely the gravitating masses extracted from lensing analysis. If we consider only the MMM and MMMC, which have been shown to be the preferred models when strong lensing is taken into account, the allowed range of  $H_0$  is more tightly constrained.

The predicted central decrements from the MMM and MMMC (for  $H_0=50 \text{ km s}^{-1} \text{ Mpc}^{-1}$ ) are  $4.8 \times 10^{-4}$  and  $4.0 \times 10^{-4}$  respectively. These are compared to the ? upper bound of  $4.0 \times 10^{-4}$ . To achieve consistency between these results,  $H_0$  must be  $> 62 \text{ km s}^{-1} \text{ Mpc}^{-1}$  for the MMM and  $> 50 \text{ km s}^{-1} \text{ Mpc}^{-1}$  for the MMMC. Lower values of the Hubble constant ensure that the predicted decrements do not lie within the ? bounds.

If the constraint of isothermality (at the fitted temperature of  $7.9_{-0.6}^{+0.7} \text{ keV}$ ) is applied, the predicted central decrement is  $3.7 \times 10^{-4}$ . When the value of  $H_0$  is allowed to vary, the range allowed by the ? bounds is  $30-105 \text{ km s}^{-1} \text{ Mpc}^{-1}$ .

This is consistent with the value of  $H_0 = 38_{-16}^{+18} \text{ km s}^{-1} \text{ Mpc}^{-1}$  derived by ?.

In summary, the constraints currently available from SZ observations combined with X-ray measurements are too weak to constrain the Hubble constant to greater accuracy than  $37\text{--}230 \text{ km s}^{-1} \text{ Mpc}^{-1}$ . This range accommodates (within errors) the previously determined values of  $24_{-10}^{+23} \text{ km s}^{-1} \text{ Mpc}^{-1}$  (?),  $65_{-25}^{+25} \text{ km s}^{-1} \text{ Mpc}^{-1}$  (?) and  $38_{-16}^{+18} \text{ km s}^{-1} \text{ Mpc}^{-1}$  (?). However, when lensing observations are introduced (which favour the MMMC model) the Hubble constant is required to be greater than  $50 \text{ km s}^{-1} \text{ Mpc}^{-1}$ . This result highlights the importance of using both non-isothermal gas models and an approach which incorporates constraints in addition to those provided by the X-ray and SZ observations alone.

## 9 DISCUSSION

We have analysed ROSAT PSPC and ASCA GIS X-ray data, fitting spherically symmetric emission models to allow the extraction of cluster properties. The use of ASCA data allows the gas temperature structure to be discerned, a significant advance over earlier instruments. The analysis procedure utilises this information by fitting a variety of parametric forms for gas density and gas temperature or gravitating mass. This avoids restricting the unknown temperature profile to a single form.

Since the analysis presented here removes the constraint of isothermality, it is important to understand the effect that this assumption has. When isothermality is applied to Equation 1, it degenerates to:

$$M_{\text{grav}}(r) = -\frac{kT_{\text{gas}}r}{G\mu m_p} \left[ \frac{d \ln \rho_{\text{gas}}(r)}{d \ln r} \right] \quad (10)$$

Hence the *shape* of the mass profile is constrained by the gas density profile alone. Since the latter is commonly taken to follow a King model, the gravitating mass distribution is forced to take the form of an isothermal sphere, with  $\rho(r) \propto r$  at large radius and flattening within a region determined by the gas core radius.

The main results are:

1) Comparison with strong lensing indicates that the previously reported discrepancy is not present when the MMM is used. A consequence of the extra mass required within the critical radius is a high central gas temperature, which may be related to the disturbed nature of the core. So, by relaxing the assumption of isothermality and using an appropriate parameterisation for the dark matter distribution (one which includes a mass cusp), the observed X-ray and strong lensing data can become consistent.

2) The suggestion, by ?, that the cD contributes a significant fraction of the cluster mass at small radius has been tested. The maximum central mass which can be added to the MMM, before the Cash statistic shifts beyond the 95% error level, is  $1.7 \times 10^{12} M_\odot$  (within 100kpc). Thus the massive galaxy required by ? is ruled out, if the underlying DM distribution follows the form of the MMM model. The effect of adding the maximum allowed central galaxy mass is to extend the DM distribution. Because of this, the MMMC is found to be more consistent than the MMM with the outer two data points extracted from the ? strong lensing analysis.

3) At larger radii, 200-1000 kpc, the projected mass profiles of the MMM and MMMC are consistent with the weak lensing results of ?. When the slope of the mass profile is considered, the MMMC becomes the favoured model, as the MMM distribution is considerably flatter than the trend of the weak lensing data. It is important to recognise that the weak lensing analysis provides only a lower limit to the actual mass distribution (since cluster mass is known to reside in the weak lensing control annulus). Hence, although the MMMC provides more mass than the weak lensing results currently allow, this discrepancy may be resolved when statistical lensing of the background galaxy population is observed to greater radii (so that a control annulus beyond the edge of the cluster can be used).

4) The steep central rise in temperature required by the MMM leads to a corresponding increase in entropy. Under these conditions the gas is likely to be convectively unstable within  $\sim 120 \text{ kpc}$ . This is either a reflection of the true physical state of the ICM or a model-dependent effect, related to the parametric forms assumed for the gas density and temperature. Evidence for the former is provided by ?, whose HRI analysis indicates the existence of central substructure, perhaps as a result of merging activity. If this is the case, the gas is likely to have been violently shock-heated, such that the assumption of equilibrium within the cluster core is no longer secure. On the other hand, the problem of convective instability is lessened with the MMMC, due to the lower fitted central temperature. In addition, replacing the King gas density profile with an NFW description can resolve the problem entirely. This is a consequence of allowing the density to rise, rather than flatten, in the cluster core.

5) Analysis of galaxy orbits provides another probe of the core region of A2218. Using the derived anisotropy of the galaxy velocities, it is possible to extract information about the gravitational potential and possible presence of substructure. Beyond the central  $1'$  region, the velocity dispersion data are consistent with the MMMC. At smaller radii, a physically reasonable solution for the anisotropy parameter cannot be attained with any of the derived X-ray mass distributions. This suggests that the central velocity dispersion has been raised to its high observed value during the violent relaxation phase of a merger event. Thus, even though the galaxy data are too poorly sampled spatially to indicate the presence of substructure, the velocity information supports the analyses of ? and ?.

6) Comparison with 2D Sunyaev-Zel'dovich observations indicates that the Hubble constant is only weakly constrained, to a range of  $37\text{--}230 \text{ km s}^{-1} \text{ Mpc}^{-1}$ . This is due to the high level of uncertainty which occurs when errors in the SZ and X-ray data are combined. More restrictive constraints on the value of  $H_0$  can be obtained if additional information is used, such as lensing observations. When the MMM and MMMC are combined with the SZ data, low values of the Hubble constant are ruled out and we find that  $H_0 > 50 \text{ km s}^{-1} \text{ Mpc}^{-1}$ . This result conflicts with the previously determined value of  $24_{-10}^{+23} \text{ km s}^{-1} \text{ Mpc}^{-1}$  (?), but agrees with the later estimate of  $65_{-25}^{+25} \text{ km s}^{-1} \text{ Mpc}^{-1}$  (?). The differences between these results, and that derived here, are dominated by several factors. The first, and most important, of these is that an unwarranted assumption has been made about the gas temperature in these earlier studies - that it is isothermal. This biases the analysis and also re-

sults in over-optimistic error estimates. Secondly, ? and ? both use (different) 1D SZ measurements, which are prone to baseline uncertainties. Third, these studies use the less accurate gas density information from Einstein, rather than ROSAT.

Note, however, that these results are all based upon the commonly made assumption that the X-ray and SZ observations can be made consistent purely by manipulating the value of  $H_0$ . If the cluster gas, at small radius, is not in hydrostatic equilibrium, this methodology may be in error.

## 10 CONCLUSIONS

Combining the above results, it appears that A2218 consists of two distinct regions. At small radii ( $\leq 1'$ ), the X-ray morphology is extremely disturbed (?) with both the strong lensing (?) and galaxy data (?) indicating the presence of bimodal structure. An X-ray model (the MMMC) consistent with the strong lensing data requires the gas temperature to rise steeply within the core, possibly at such a high rate that the gas is convectively unstable. When this model is combined with the observed galaxy data, a physical solution cannot be obtained for galaxy orbits within the core. Taken together, these results suggest that A2218 has recently undergone a merger, shock-heating the gas and disturbing the equilibrium of the components within the cluster. This explains the lack of a cooling flow in the system.

Outside the core, our results show that the data can be consistently interpreted on the basis of a cluster in equilibrium. The gas temperature falls to  $< 10$  keV, consistent with the observed galaxy velocity dispersion, and the gas entropy increases with radius. The MMMC provides a mass profile consistent with both the outer two strong lensing points and the weak lensing mass profile (with the proviso that the latter is likely to represent an underestimate of the true mass profile). When the MMMC is combined with the galaxy velocity data, a physical solution for the galaxy orbits is recovered. The SZ data, which are sensitive to the gas pressure at large radius, are consistent with the MMMC when  $H_0 \geq 50$  km s $^{-1}$  Mpc $^{-1}$ .

Thus, while it is premature to regard a model such as the MMMC as a complete description of the physical structure of A2218, it does appear to explain all the data available beyond the disturbed core. To probe further, more detailed X-ray and weak lensing observations are required.

One of the principal conclusions to be drawn from the present analysis is that it is dangerous to assume an isothermal ICM without supporting evidence. This can lead to biased conclusions and underestimated errors.

## ACKNOWLEDGMENTS

We would like to thank Gordon Squires for providing us with his weak lensing mass profiles, Mike Jones for his information on interferometric Sunyaev-Zel'dovich analysis and Paul Nulsen & Priya Natarajan for helpful discussions. In addition, we wish to the referee, Hans Boehringer, for valuable suggestions which improved the paper.

DBC and ISH acknowledge the financial support of the UK Particle Physics and Astronomy Research Council

(PPARC). Computational work was done on the Birmingham node of the PPARC funded Starlink network.

This paper has been produced using the Royal Astronomical Society/Blackwell Science L<sup>A</sup>T<sub>E</sub>X style file.